Full Scale Regression-based Injection Coefficients for Panchromatic Sharpening

Gemine Vivone, *Member, IEEE*, Rocco Restaino, *Member, IEEE*, and Jocelyn Chanussot, *Fellow, IEEE*

***Abstract*—Pansharpening is usually related to the fusion of a high spatial resolution but low spectral resolution (panchromatic) image with a high spectral resolution but low spatial resolution (multispectral) image. The calculation of injection coefficients through regression is a very popular and powerful approach. These coefficients are usually estimated at reduced resolution. In this paper, the estimation of the injection coefficients at full resolution for regression-based pansharpening approaches is proposed. To this aim, an iterative algorithm is proposed and studied. Its convergence, whatever the initial guess, is demonstrated in all the practical cases and the reached asymptotic value is analytically calculated. The performance is assessed both at reduced resolution and at full resolution on four datasets acquired by the IKONOS sensor and the WorldView-3 sensor. The proposed full scale approach always shows the best performance with respect to the benchmark consisting of state-of-the-art pansharpening methods.**

***Index Terms*—Iterative Methods, Full Scale Estimation, Pansharpening, Data Fusion, Remote Sensing.**

I. Introduction

Satellite Earth observation finds application in many human activities, allowing the continuous exploration and analysis of large zones of the globe surface. Environmental change detection, agriculture monitoring, weather forecasting, topography mapping are only few examples of problems currently approached through remotely sensed data [1]. The effectiveness of the solutions based on satellite data is strictly related to the accurateness of images reproducing the illuminated Earth surface area, commonly stated in terms of spatial and spectral resolutions. However, the collection of data exploiting a sole sensor characterized by high quality in both the domains is precluded by physical constraints and by the limited transmission and processing capabilities for devices on board of satellites.

Data fusion approaches overcome these limitations allowing the combination of images with different characteristics [2]. For that reason, remotely sensed data providers have increased the offer of high level products that typically exploit the availability of images acquired in similar frequency ranges by sensors mounted on the same platform. A successful application of these techniques is the *pansharpening*, namely the fusion of two optical images collected by a panchromatic (PAN) and a multispectral (MS) sensor, respectively, which are present on board of many modern satellites, as, for instance, Pléiades, QuickBird and the WorldView (WV) family.

As a matter of fact, the pansharpened products are now widely employed for aiding visual interpretation of data, as it happens in software platforms such as Google Earth and Microsoft Bing. In addition, several scientific contributions have been devoted to demonstrate the performance gain achievable through the use of pansharpened images in many applications, such as spatial feature extraction [3], crop monitoring [4], snow mapping [5], and change detection [6], [7].

A. Related Works

In order to meet this demand, the scientific literature has been populated by many papers that are surveyed in review papers [8], [9], [10], [11], and a comprehensive book [2]. These reviews clearly show the current availability of a large number of approaches, which constitute the well-known class of "second generation" methods (optimized algorithms often exploiting the sensor's physical knowledge), natural consequence of the first group of techniques proposed in some seminal papers [12], [13], [14], [15]. To date, second generation approaches constitute the most used class of methods, since they achieve an adequate balance between quality of pansharpened products and computational burden. In fact, a further (third) generation of high-performance pansharpening approaches has recently emerged including sophisticated methods that require time demanding optimization phases. A wide group is constituted by methods that recast pansharpening as an inverse problem. The PAN and MS images are seen as coarse measurements of an ideal high resolution MS image, which is estimated through penalization terms based on spectral correlation [16], total variation [17], [18], [19], representation coefficient sparsity [20], [21], [22], or properly formulated specific assumptions [23]. Machine learning methods represent another very promising class of new techniques that have received a substantial impulse by the abrupt growth of computer computational capabilities caused by GPUs [24].

Classical second generation methods are all sons of a single theoretical formulation[1]. They are typically distinguished into two main groups that yield images with complementary features:

- The *spectral class* includes techniques that involve the substitution of a component of the original MS image in

G. Vivone and R. Restaino are with the Department of Information Engineering, Electrical Engineering and Applied Mathematics, University of Salerno, 84084 Fisciano, Italy (e-mails: gvivone@unisa.it; restaino@unisa.it).
J. Chanussot is with Univ. Grenoble Alpes, CNRS, Grenoble INP, GIPSA-lab, 38000 Grenoble, France (e-mail: jocelyn.chanussot@gipsa-lab.grenoble-inp.fr).

[1]See also (1) in Sect. II of the current paper.

a transformed domain. For this reason, they are denoted as *component substitution* (CS) methods. Notable examples are the *intensity-hue-saturation* (IHS) [14], [25], the *principal component substitution* (PCS) [13], [26], [27], the *Gram-Schmidt* (GS) spectral sharpening [15], belonging to the first generation methods, the *GS adaptive* approach [28] and the band-dependent spatial detail (BDSD) [29], which are prototypes of the second generation approaches.

- The *spatial class* is composed by algorithms that operate directly in the spatial domain through the application of one of multiple linear shift-invariant digital filters. The latter yield a more or less complex multiscale decomposition of the signal, hence the name of *multiresolution analysis* (MRA) methods. Widespread archetypes rely upon box filters (*smoothing filter-based intensity modulation* (SFIM) [30], [31]), *decimated wavelet transform* (DWT) [32], *undecimated wavelet transform* (UDWT) [33], *"à-trous" wavelet transform* (ATWT) [34], *Laplacian pyramid* (LP) [35], *contourlet* [36], *curvelet* [37] and *morphological operators* [38]. More advanced implementations have been also proposed for MRA methods, yielding second generation algorithms that include also the winner of the 2006 GRS-S fusion contest [39].

Previous works have shown that the CS methods are more suited to produce visually appealing images reducing spatial distortions, whereas MRA methods are more appropriate to preserve the spectral features of the original MS image [8]. Furthermore the two classes are characterized by complementary properties in terms of robustness to spatial and temporal misalignments [40].

Approaches belonging to the second generation class split the pansharpening problem into two sub-problems: i) the detail extraction from the PAN image and ii) the detail injection, through the multiplication by injection coefficients, into the upsampled original MS image. Thus, pansharpening approaches differ from the way to extract details (which classifies methods into either CS or MRA classes) and to set the injection coefficients.

High performance second generation algorithms are often characterized by injection coefficients estimated given the image pair at hand. Noticeable examples are MRA methods employing the *high-pass modulation* (HPM) injection scheme [1] together with a wavelet decomposition (ATWT-HPM) [41], or with a generalized Laplacian pyramid (GLP) based on Gaussian filters matching the modulation transfer function (MTF) of the MS sensor (MTF-GLP-HPM) [42], or with a nonlinear decomposition employing morphological half gradients [43]. Other state-of-the-art approaches involving the injection coefficient estimation phase are represented by the two Gram-Schmidt versions proposed in [44], namely the *GS mode 2* (GS2) (named *MTF-GLP context-based decision* (MTF-GLP-CBD) in [39], [8]), and the *GS adaptive* (GSA) [28], belonging to the MRA class and the CS class, respectively. The latter methods are often called *regression-based* (or *projective*) methods, since the coefficient estimation is performed by linear regression between the MS channels and the PAN image. Local version have been proposed and assessed in [45] and [46]. Another central approach requiring the estimation of coefficients is the BDSD algorithm [29], in which this step is carried out in conjunction with the detail extraction phase; a clustering-based implementation of the BDSD has been presented in [47].

The estimation of injection coefficients is a crucial task to which we devote this study. All the proposed approaches encompass the comparison of the characteristics of the MS channels and those of the PAN image, either on a pixel basis (HPM methods), or on a channel basis (regression-based methods, BDSD), or on groups of pixels (segmentation and clustering based approaches). The crucial issue in this process is constituted by the different resolutions of the available images that preclude a direct comparison of the contained information. The common solution consists in working at the original MS resolution, where the low spatial resolution PAN image is obtained either by spatially filtering the original PAN image (MRA methods) or by properly combining the different MS bands (CS methods). We will name the techniques employing this protocol as *reduced scale* (RS) approaches from hereon.

B. Paper Contribution

In this work, we propose strategies that are able to deal with the injection coefficient estimation problem at *full scale* (FS). More specifically, we elaborate on the exemplary MTF-GLP-CBD approach [39], in which the details of the PAN images are extracted through a Gaussian-shaped low pass filter. In the original approach the injection coefficients are calculated as the slope of the regression line (i.e. ratio between sample covariance and sample variance) between the MS channel and the PAN image. We deeply investigate in this paper the opportunity of calculating the same coefficients at FS and propose multiple approaches for performing this task.

The first straightforward (two-step) method consists in defining the injection coefficients as the slope of the regression line between the original PAN image and a high resolution MS image (i.e. a guess image) obtained by combining the available MS and PAN images through a pansharpening algorithm. The iteration of this concept leads to an iterative algorithm. In other terms, at each iteration the role of the high resolution MS image required for computing the injection coefficients is played by the fused product obtained at the previous step. As in the case of the first proposed method, a simple pansharpening algorithm is employed to obtain the algorithm initialization. The study of the iterative approach shows that, under very mild conditions typically satisfied in all the practical cases, the solution converges to a fixed point whatever the initialization. More crucially, the asymptotic value of the coefficients admits a closed-form expression, which allows us an immediate calculation without performing the execution of time-consuming iterations. These asymptotic coefficients can be seen as a new regression-based injection rule at FS. Thus, the study is completed by the analysis of the relationship between the new FS and the state-of-the-art RS regression-based injection rules.

The proposed FS strategies are fully assessed by employing two different datasets, acquired by the IKONOS and the

WorldView-3 sensors, which are characterized by significantly different features (e.g. a different number of MS spectral channels). Both the reduced resolution and the full resolution assessment procedures [8] are used to assess the performance. Quantitative outcomes demonstrate the superiority of the proposed approaches with respect to existing methods. Whereas the two-step procedure turns out to be suitable only when the preliminary pansharpening step is performed through a high performance algorithm, the iterative approach always yields appreciable results that, thanks to the closed-form solution, are accompanied by a low computational burden.

Summarizing, in this work the suitability of FS procedures for estimating the injection coefficients is stated and assessed, obtaining the following main results:

- A simple two-step pansharpening algorithm is proposed and used as a research baseline;
- An iterative procedure for successively improving the quality of both the injection coefficient estimation and the fused product is designed and studied pointing out the (very mild) conditions assuring the asymptotic existence of a closed-form expression of the injection coefficients whatever the initialization of the iterative procedure.
- A study on the relationship between the novel formula obtained at FS and the classical one calculated at RS has been performed.
- The proposed approaches have been assessed on real data by means of the most credited validation protocols, working both at reduced and at full resolution.

C. Paper Outline

The remaining of the paper is organized as follows. In Sect. II we formalize the problem at hand from the mathematical point of view. We clarify the adopted notation and illustrate the formulation encompassing the main classical pansharpening approaches. The injection coefficient estimation problem is reported in Sect. II-A detailing the iterative solution proposed in this paper; the closed form expression of the FS injection coefficients is derived in Sect. II-B; for the sake of clarity we defer the proofs of some details to App. A. Sect. III shows the numerical results of the proposed approach with respect to state-of-the-art methods. Finally, conclusions are drawn in Sect. IV.

II. The Pansharpening Problem and Injection Coefficient Estimation

In this paper, the following mathematical notation is adopted. An image is generally denoted by bold uppercase, i.e. $\mathbf{X}$. Accordingly, the panchromatic (PAN) image is a $N \times M$ two-dimensional array denoted by $\mathbf{P}$ with N and M indicating the number of rows and columns of the PAN image, respectively. Whereas, the multispectral (MS) image is a $N/R \times M/R \times K$ three-dimensional array denoted by $\mathbf{MS} = \{\mathbf{MS}_k\}_{k=1\ldots,K}$, where $\mathbf{MS}_k$ indicates the k-th spectral channel, K is the number of spectral bands, and R is the resolution ratio between the original MS and the PAN images.

Formally, the goal of pansharpening is the generation of a $N \times M \times K$ MS image $\widehat{\mathbf{MS}} = \{\widehat{\mathbf{MS}}_k\}_{k=1\ldots,K}$, which represents an estimate of the ideal MS image at spatial resolution of $\mathbf{P}$, hereafter indicated as $\mathbf{GT} = \{\mathbf{GT}_k\}_{k=1\ldots,K}$. The reference $N \times M \times K$ image $\mathbf{GT}$ is unavailable in practice. Furthermore, we denote by $\widetilde{\mathbf{MS}} = \{\widetilde{\mathbf{MS}}_k\}_{k=1\ldots,K}$, the $N \times M \times K$ MS image obtained by simply upsampling $\mathbf{MS}$ to the PAN scale. It is worth to be remarked that the proposed approaches are related to the fusion of spatially aligned MS and PAN products, thus considering the critical issue of the geometrical co-registration of the input data already solved after the upsampling step.

Classical algorithms, to which we refer in this paper, can be synthesized by a single channel-wise equation [8]

$$\widehat{\mathbf{MS}}_k = \widetilde{\mathbf{MS}}_k + g_k \left(\mathbf{P}^k - \mathbf{P}_L^k\right), \tag{1}$$

wherein g_k is the k-th injection coefficient and $\mathbf{P}_L$ is a low resolution version of $\mathbf{P}$. The superscript k indicates the dependence on the band k. The way to produce the PAN low spatial resolution version $\mathbf{P}_L^k$ distinguishes the two main classes of pansharpening approaches. More specifically, component substitution (CS) methods exploit a unique PAN low resolution version, i.e. $\mathbf{P}_L^k = \mathbf{I}$ for all k, where the intensity component $\mathbf{I}$, which is a function of the MS image, is usually calculated as follows

$$\mathbf{I} = \sum_{i=1}^{K} \alpha_i \widetilde{\mathbf{MS}}_i. \tag{2}$$

The coefficients $\{\alpha_i\}_{i=1,\ldots,K}$ in (2) can be estimated through a minimum mean square error (MMSE) procedure [28]. Thus, the fused image $\widehat{\mathbf{MS}}_k$ in (1) is simply obtained by substituting $\mathbf{P}_L^k$ with the intensity component defined in (2) and $\mathbf{P}^k$ with $\mathbf{P}$ for all k.

Regarding the multi-resolution analysis (MRA) class, $\mathbf{P}^k$ could be function of the spectral channel k. Indeed, some approaches, see e.g. [8], require a preliminary equalization step between $\mathbf{P}$ and $\widetilde{\mathbf{MS}}_k$ getting a PAN image function of k, i.e. $\mathbf{P}^k$. $\mathbf{P}_L^k$ is derived through a multi-scale decomposition of $\mathbf{P}^k$, which can be band-dependent (i.e. different spatial filters applied to different spectral bands). Thus, several MRA approaches can be achieved by exploiting different decomposition methods. The simplest way consists in filtering $\mathbf{P}^k$ through a linear time invariant system, with impulse response h_k, namely in defining $\mathbf{P}_L^k$ as $\mathbf{P}_L^k = \mathbf{P}^k * h_k$.

Despite its simplicity, this instance leads to state-of-the-art performance if the amplitude response of h_k is matched with the MS sensor's modulation transfer function (MTF) of the k-th spectral channel. A Gaussian filter is typically employed for approximating the desired system, setting its unique parameter (i.e. its standard deviation) for matching the values of the amplitude response at the Nyquist frequency. The corresponding method is referred to as generalized Laplacian pyramid (GLP) [48] with MTF-matched filter [44].

A. Reduced and Full Scale Injection Coefficients

In this section, for sake of brevity, we focus attention on the powerful GLP with MTF-matched filter approach, which

is here denoted as *GLP-Reg*, thus referring to a GLP approach matched with the MS sensor's MTF exploiting a regression-based injection model proposed in [28] for the CS methods. This approach is well-known in the literature, usually called GLP with context-based decision (GLP-CBD) [48], [44], [39], [8], and often reaching state-of-the-art performance [39], [8]. However, all the considerations about the full scale injection coefficient estimation are general and can be easily extended to the other regression-based CS/MRA approaches.

Generally speaking, it is worth to be remarked that regression-based injection models as in [28], [8] are always defined at reduced scale (RS), i.e. the injection coefficients $\{g_k\}_{k=1,\dots,K}$ are calculated at MS spatial resolution, where the MS image is available and the low resolution version of the PAN product, $\mathbf{P}_L$, can be straightforwardly generated (see some above-mentioned examples). Hence, we have that the injection coefficients $\{g_k\}_{k=1,\dots,K}$ for a linear regression-based model at RS are equal to

$$g_k^{RS} = \frac{\operatorname{cov}\left(\widetilde{\mathbf{MS}}_k, \mathbf{P}_L^k\right)}{\operatorname{var}\left(\mathbf{P}_L^k\right)}, \tag{3}$$

in which $\operatorname{cov}(\mathbf{X}, \mathbf{Y})$ is the sample covariance of images $\mathbf{X}$ and $\mathbf{Y}$ and $\operatorname{var}(\mathbf{X})$ is the sample variance of image $\mathbf{X}$. In other words, the injection coefficients are equal to the projection of the upsampled images $\widetilde{\mathbf{MS}}_k$ on the low resolution version $\mathbf{P}_L^k$ of the PAN image. For this reason, this injection model is also named *projective* injection model. We can easily note from (3) that when a projective (regression-based) injection model is used, no preliminary equalization step is required for properly fusing PAN and MS images [49].

Under the use of a RS injection model, there is a crucial assumption of scale invariance. Indeed, the advisability of this definition strictly depends on the similarity of the value calculated through (3) and the projection of the reference image $\mathbf{GT}_k$ on the PAN image $\mathbf{P}^k$

$$g_k^{GT} = \frac{\operatorname{cov}\left(\mathbf{GT}_k, \mathbf{P}^k\right)}{\operatorname{var}\left(\mathbf{P}^k\right)}. \tag{4}$$

In this work we investigate the possibility of removing this scale invariance assumption by finding a reasonable full scale approximation to the unfeasible (due to the absence of a reference image that is the goal of pansharpening) expression (4). As far as we know, this is the first attempt to critically analyze this scale invariance assumption commonly performed for estimating injection coefficients in pansharpening.

To overcome this assumption of scale invariance, the main idea is, instead of degrading the PAN at spatial resolution of the MS image, to synthesize a MS image at PAN spatial resolution, i.e. at full scale (FS). Thus, a two-steps procedure can be applied: i) a synthesized high spatial resolution MS image (guess image), say $\widehat{\mathbf{MS}}^{(0)}$, is calculated; ii) equation (4) is used by substituting $\mathbf{GT}$ with $\widehat{\mathbf{MS}}^{(0)}$, namely, the injection coefficients become

$$g_k^{FS,0} = \frac{\operatorname{cov}\left(\widehat{\mathbf{MS}}_k^{(0)}, \mathbf{P}^k\right)}{\operatorname{var}\left(\mathbf{P}^k\right)}. \tag{5}$$

The guess image $\widehat{\mathbf{MS}}_k^{(0)}$ is an instance of a high spatial resolution MS image. Thus, a first rough estimation can be simply provided by the upsampled MS image, i.e. $\widetilde{\mathbf{MS}}$. This is done at no computational cost (product already used in the fusion rule (1)). Instead, more powerful solutions from a performance point of view are provided by pansharpening fusion algorithms belonging to CS and MRA classes. Generally speaking, the more the similarity between the fused image and the reference image, the better the estimation of the injection coefficients thus generating a higher performance final fused product.

Remark: It is worth to be remarked that since the guess (pansharpened) image has to be used in the detail injection model, the similarity between the guess (pansharpened) image and the reference image is intended spectrally only (the expected impact of a spatial distortion in the fused product is low compared to the same amount of spectral distortion).

An improved version of the high resolution MS image estimate can be produced through (1) using the coefficients $g_k^{FS,0}$, i.e.

$$\widehat{\mathbf{MS}}_k^{(1)} = \widetilde{\mathbf{MS}}_k + g_k^{FS,0}\left(\mathbf{P}^k - \mathbf{P}_L^k\right). \tag{6}$$

The described strategy can be iterated for a fixed number of iterations N_{iter}. Thus, we have

for $j = 0, \dots, N_{iter} - 1$ **do**

- Calculate the injection coefficients $g_k^{FS,j}$ as

$$g_k^{FS,j} = \frac{\operatorname{cov}\left(\widehat{\mathbf{MS}}_k^{(j)}, \mathbf{P}^k\right)}{\operatorname{var}\left(\mathbf{P}^k\right)} \tag{7}$$

- Fuse MS and PAN images using the injection coefficients $g_k^{FS,j}$

$$\widehat{\mathbf{MS}}_k^{(j+1)} = \widetilde{\mathbf{MS}}_k + g_k^{FS,j}\left(\mathbf{P}^k - \mathbf{P}_L^k\right) \tag{8}$$

end

Reasonably, the estimation of the injection coefficients over the iterations is better and better due to the fact that the guess image is less and less roughly estimated. Thus, a higher and higher quality of the fused image is expected, at the price of a monotonic increase of the algorithm complexity.

B. Closed Form FS Iterative Procedure

The crucial result of this study is that applying the iterated procedure to the *GLP-Reg* approach leads to a fixed point admitting the following closed form expression:

$$g_k^{FS,\infty} = \frac{\operatorname{cov}\left(\widetilde{\mathbf{MS}}_k, \mathbf{P}^k\right)}{\operatorname{cov}\left(\mathbf{P}_L^k, \mathbf{P}^k\right)}. \tag{9}$$

Therefore, the asymptotic fused image related to the injection coefficients $g_k^{FS,\infty}$ can be easily calculated in one step without the need of the iterative algorithm. This strongly reduces the computational burden that is thus comparable to the other GLP classical pansharpening approaches. Hence, the final fused

image $\widehat{\mathbf{MS}}_k$ is achieved by (9) using the following fusion rule

$$\widehat{\mathbf{MS}}_k = \widehat{\mathbf{MS}}_k^{(\infty)} = \widetilde{\mathbf{MS}}_k + g_k^{FS,\infty}\left(\mathbf{P}^k - \mathbf{P}_L^k\right). \tag{10}$$

The expression (9) is straightforwardly derived by the initial value

$$g_k^{FS,0} = \frac{\operatorname{cov}(\widetilde{\mathbf{MS}}_k, \mathbf{P}^k)}{\operatorname{var}(\mathbf{P}^k)}. \tag{11}$$

Indeed, if the relation

$$g_k^{FS,n-1} = \frac{\operatorname{cov}(\widetilde{\mathbf{MS}}_k, \mathbf{P}^k)}{\operatorname{var}(\mathbf{P}^k)} \sum_{i=0}^{n-1}\left(1 - \frac{\operatorname{cov}(\mathbf{P}_L^k, \mathbf{P}^k)}{\operatorname{var}(\mathbf{P}^k)}\right)^i, \tag{12}$$

holds at iteration $n-1$, the corresponding formula at iteration n

$$g_k^{FS,n} = \frac{\operatorname{cov}(\widetilde{\mathbf{MS}}_k, \mathbf{P}^k)}{\operatorname{var}(\mathbf{P}^k)} \sum_{i=0}^{n}\left(1 - \frac{\operatorname{cov}(\mathbf{P}_L^k, \mathbf{P}^k)}{\operatorname{var}(\mathbf{P}^k)}\right)^i \tag{13}$$

can be demonstrated by the following steps

$$\begin{aligned}
g_k^{FS,n} =& \frac{\operatorname{cov}(\widehat{\mathbf{MS}}_k^{(n)}, \mathbf{P}^k)}{\operatorname{var}(\mathbf{P}^k)} \\
=& \frac{\operatorname{cov}\left(\left[\widetilde{\mathbf{MS}}_k + g_k^{FS,n-1}\left(\mathbf{P}^k - \mathbf{P}_L^k\right)\right], \mathbf{P}^k\right)}{\operatorname{var}(\mathbf{P}^k)} \\
=& \frac{\operatorname{cov}(\widetilde{\mathbf{MS}}_k, \mathbf{P}^k)}{\operatorname{var}(\mathbf{P}^k)} + \left[\frac{\operatorname{cov}(\widetilde{\mathbf{MS}}_k, \mathbf{P}^k)}{\operatorname{var}(\mathbf{P}^k)}\right. \\
& \left. \times \sum_{i=0}^{n-1}\left(1 - \frac{\operatorname{cov}(\mathbf{P}_L^k, \mathbf{P}^k)}{\operatorname{var}(\mathbf{P}^k)}\right)^i\right] \frac{\operatorname{cov}\left(\left(\mathbf{P}^k - \mathbf{P}_L^k\right), \mathbf{P}^k\right)}{\operatorname{var}(\mathbf{P}^k)} \\
=& \frac{\operatorname{cov}(\widetilde{\mathbf{MS}}_k, \mathbf{P}^k)}{\operatorname{var}(\mathbf{P}^k)} \\
& + \left[\frac{\operatorname{cov}(\widetilde{\mathbf{MS}}_k, \mathbf{P}^k)}{\operatorname{var}(\mathbf{P}^k)} \sum_{i=1}^{n}\left(1 - \frac{\operatorname{cov}(\mathbf{P}_L^k, \mathbf{P}^k)}{\operatorname{var}(\mathbf{P}^k)}\right)^i\right] \\
=& \frac{\operatorname{cov}(\widetilde{\mathbf{MS}}_k, \mathbf{P}^k)}{\operatorname{var}(\mathbf{P}^k)} \sum_{i=0}^{n}\left(1 - \frac{\operatorname{cov}(\mathbf{P}_L^k, \mathbf{P}^k)}{\operatorname{var}(\mathbf{P}^k)}\right)^i.
\end{aligned} \tag{14}$$

Since (12) reduces to (11) for $n = 1$, (13) is valid for all $n \geq 0$ and thus the asymptotic value is given by

$$\begin{aligned}
g_k^{FS,\infty} =& \lim_{n\to\infty} g_k^{FS,n} \\
=& \frac{\operatorname{cov}(\widetilde{\mathbf{MS}}_k, \mathbf{P}^k)}{\operatorname{var}(\mathbf{P}^k)} \sum_{i=0}^{\infty}\left(1 - \frac{\operatorname{cov}(\mathbf{P}_L^k, \mathbf{P}^k)}{\operatorname{var}(\mathbf{P}^k)}\right)^i \\
\overset{(a)}{=}& \frac{\operatorname{cov}(\widetilde{\mathbf{MS}}_k, \mathbf{P}^k)}{\operatorname{var}(\mathbf{P}^k)} \frac{1}{1 - \left[1 - \frac{\operatorname{cov}(\mathbf{P}_L^k, \mathbf{P})}{\operatorname{var}(\mathbf{P}^k)}\right]} \\
=& \frac{\operatorname{cov}(\widetilde{\mathbf{MS}}_k, \mathbf{P}^k)}{\operatorname{var}(\mathbf{P}^k)} \frac{1}{\frac{\operatorname{cov}(\mathbf{P}_L^k, \mathbf{P}^k)}{\operatorname{var}(\mathbf{P}^k)}} = \frac{\operatorname{cov}(\widetilde{\mathbf{MS}}_k, \mathbf{P}^k)}{\operatorname{cov}(\mathbf{P}_L^k, \mathbf{P}^k)}
\end{aligned} \tag{15}$$

where (a) holds if

$$\left|1 - \frac{\operatorname{cov}(\mathbf{P}_L^k, \mathbf{P}^k)}{\operatorname{var}(\mathbf{P}^k)}\right| < 1 \Leftrightarrow 0 < \frac{\operatorname{cov}(\mathbf{P}_L, \mathbf{P}^k)}{\operatorname{var}(\mathbf{P}^k)} < 2. \tag{16}$$

This condition can be rewritten in explicit form by noting that

$$\begin{aligned}
\frac{\operatorname{cov}(\mathbf{P}_L^k, \mathbf{P}^k)}{\operatorname{var}(\mathbf{P}^k)} &= \frac{\rho(\mathbf{P}_L^k, \mathbf{P}^k)\operatorname{std}(\mathbf{P}_L^k)\operatorname{std}(\mathbf{P}^k)}{\operatorname{var}(\mathbf{P}^k)} \\
&= \rho(\mathbf{P}_L^k, \mathbf{P}^k)\frac{\operatorname{std}(\mathbf{P}_L^k)}{\operatorname{std}(\mathbf{P}^k)}
\end{aligned} \tag{17}$$

where $\operatorname{std}(\mathbf{X}) = \sqrt{\operatorname{var}(\mathbf{X})}$ is the standard deviation of the image $\mathbf{X}$ and $\rho(\mathbf{X}, \mathbf{Y}) = \operatorname{cov}(\mathbf{X}, \mathbf{Y}) / (\operatorname{std}(\mathbf{X})\operatorname{std}(\mathbf{Y}))$ is the *Pearson correlation coefficient* between images $\mathbf{X}$ and $\mathbf{Y}$. Thus, condition (16) can be easily verified in the practice since the standard deviation of $\mathbf{P}_L^k$ is smaller than that of $\mathbf{P}^k$, being $\mathbf{P}_L^k$ the low-pass filtered version of $\mathbf{P}^k$, i.e.

$$0 < \frac{\operatorname{std}(\mathbf{P}_L^k)}{\operatorname{std}(\mathbf{P}^k)} < 1 \tag{18}$$

and the images $\mathbf{P}_L^k$ and $\mathbf{P}^k$ are positively correlated, namely

$$0 < \rho(\mathbf{P}_L^k, \mathbf{P}^k) < 1. \tag{19}$$

Noticeably, the same value is obtained by starting from any initial value (guess image), as detailed in Appendix A.

The full scale expression (9) admits also the equivalent form

$$g_k^{FS,\infty} = \frac{\operatorname{cov}(\widetilde{\mathbf{MS}}_k, \mathbf{P}^k)}{\operatorname{cov}(\mathbf{P}_L^k, \mathbf{P}^k)} = \frac{\rho(\widetilde{\mathbf{MS}}_k, \mathbf{P}^k)}{\rho(\mathbf{P}_L^k, \mathbf{P}^k)} \frac{\operatorname{std}(\widetilde{\mathbf{MS}}_k)}{\operatorname{std}(\mathbf{P}_L^k)} \tag{20}$$

and becomes similar to the reduced scale value

$$g_k^{RS} = \frac{\operatorname{cov}(\widetilde{\mathbf{MS}}_k, \mathbf{P}_L^k)}{\operatorname{var}(\mathbf{P}_L^k)} = \rho(\widetilde{\mathbf{MS}}_k, \mathbf{P}_L^k)\frac{\operatorname{std}(\widetilde{\mathbf{MS}}_k)}{\operatorname{std}(\mathbf{P}_L^k)} \tag{21}$$

for $\rho(\mathbf{P}_L^k, \mathbf{P}^k) \to 1$. Indeed, if $\rho(\mathbf{P}_L^k, \mathbf{P}^k) \to 1$, we have also that $\rho(\widetilde{\mathbf{MS}}_k, \mathbf{P}_L^k) \to \rho(\widetilde{\mathbf{MS}}_k, \mathbf{P}^k)$. If we consider the extreme case of $\rho(\mathbf{P}_L^k, \mathbf{P}^k) = 1$ (perfect positive linear correlation between $\mathbf{P}_L^k$ and $\mathbf{P}^k$), then$\rho(\widetilde{\mathbf{MS}}_k, \mathbf{P}_L^k) = \rho(\widetilde{\mathbf{MS}}_k, \mathbf{P}^k)$[2]. Thus, since $\rho(\mathbf{P}_L^k, \mathbf{P}^k) = 1$ and $\rho(\widetilde{\mathbf{MS}}_k, \mathbf{P}_L^k) = \rho(\widetilde{\mathbf{MS}}_k, \mathbf{P}^k)$, the equality between (20) and (21) is verified.

III. Experimental Results

Tests have been carried out on four datasets acquired by two different instruments of different generations. Indeed, data acquired by the IKONOS sensor (4 MS spectral bands) and by the WorldView-3 (8 MS spectral bands) are considered in this work. Both reduced and full resolution validations are exploited to assess the performance of the proposed approaches. State-of-the-art methods belonging to the CS and MRA classes are considered as benchmark. The tests point at analyzing the benefits of the proposed full resolution regression-based strategy with respect to the benchmark.

[2]Let us suppose we have a variable $\tilde{\mathbf{Y}}$ that has a perfect positive linear correlation with another variable $\mathbf{Y}$, i.e. $\rho(\mathbf{Y}, \tilde{\mathbf{Y}}) = 1$. Hence, we can write that

$$\tilde{\mathbf{Y}} = a\mathbf{Y} + b, \tag{22}$$

where a and b are two coefficients, with $a > 0$ due to the positive correlation between the two variables.

By using (22), the Pearson correlation coefficient $\rho(\mathbf{X}, \tilde{\mathbf{Y}})$ between a generic variable $\mathbf{X}$ and $\tilde{\mathbf{Y}}$ can be written as

$$\rho(\mathbf{X}, \tilde{\mathbf{Y}}) = \frac{a\operatorname{cov}(\mathbf{X}, \mathbf{Y})}{|a|\operatorname{std}(\mathbf{X})\operatorname{std}(\mathbf{Y})}. \tag{23}$$

Thus, since $a > 0$ and considering the the Pearson correlation coefficient definition, we have from (23) that $\rho(\mathbf{X}, \tilde{\mathbf{Y}}) = \rho(\mathbf{X}, \mathbf{Y})$.

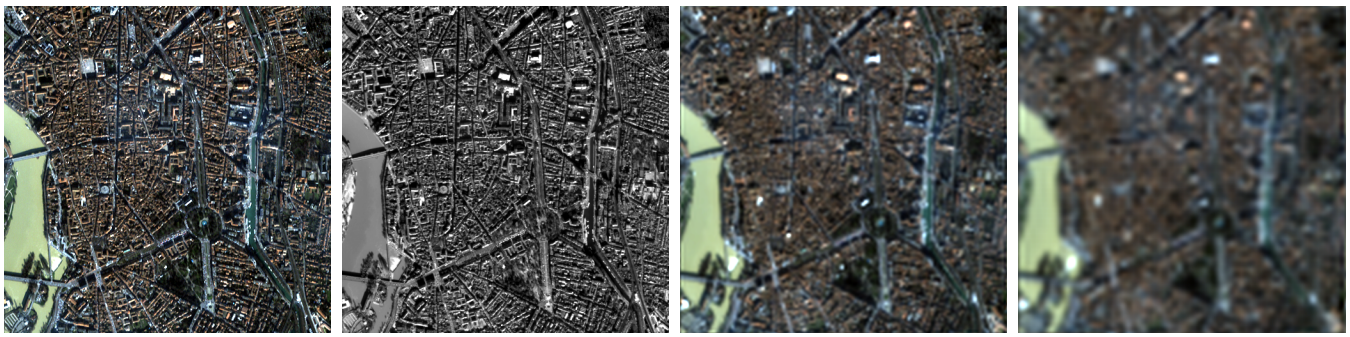

(a) (b) (c) (d)

Fig. 1: *Toulouse dataset*: (a) GT; (b) PAN; (c) MS with $R = 4$; (d) MS with $R = 8$.

(a) (b) (c)

Fig. 2: *Rio dataset*: (a) GT; (b) MS; (c) PAN.

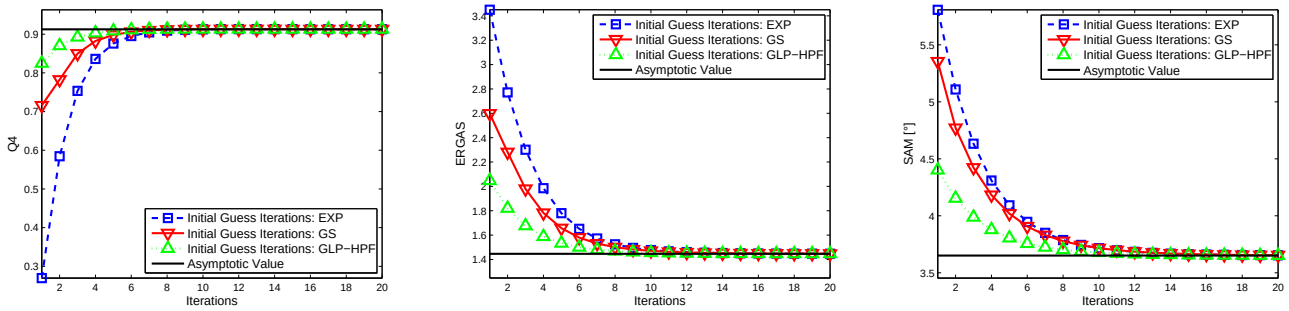

(a) (b) (c)

Fig. 3: (a) Q4, (b) ERGAS, and (c) SAM over iterations for the *Toulouse dataset* with $R = 8$.

A. Datasets

1) *Toulouse dataset*: An IKONOS image has been acquired over the urban area of Toulouse, France. The four MS bands, acquired in the visible near-infrared (VNIR) spectral range (blue, green, red, and near-infrared (NIR) bands), have 4 m spatial resolution. The panchromatic camera captures images with a spatial resolution of 1 m. Thus, the spatial resolution ratio R between MS and PAN is 4. The format of the data is spectral radiance with 11-bits word-length. We consider two test cases exploiting Wald's protocol [50]: i) $R = 4$ emulating the real spatial resolution ratio between MS and PAN; ii) $R = 8$ simulating a greater spatial difference between MS and PAN, thus stressing the need of full resolution injection coefficients. The size of the datasets in both the cases is 512×512 pixels. An overview of the used images is in Fig. 1.
2) *Rio dataset*: A WorldView-3 image has been acquired over the urban area of Rio De Janeiro, Brazil. The *Rio dataset* is characterized by the acquisition of 8 MS spectral bands in the VNIR spectrum (coastal, blue, green, yellow, red, red edge, NIR1, and NIR2) and a panchromatic image. The spatial sampling interval (SSI) is about 1.2 m for MS and about 0.3 m for PAN. Thus, R is equal to 4, again. The data format is spectral radiance with 11-bits resolution. We consider two test cases:

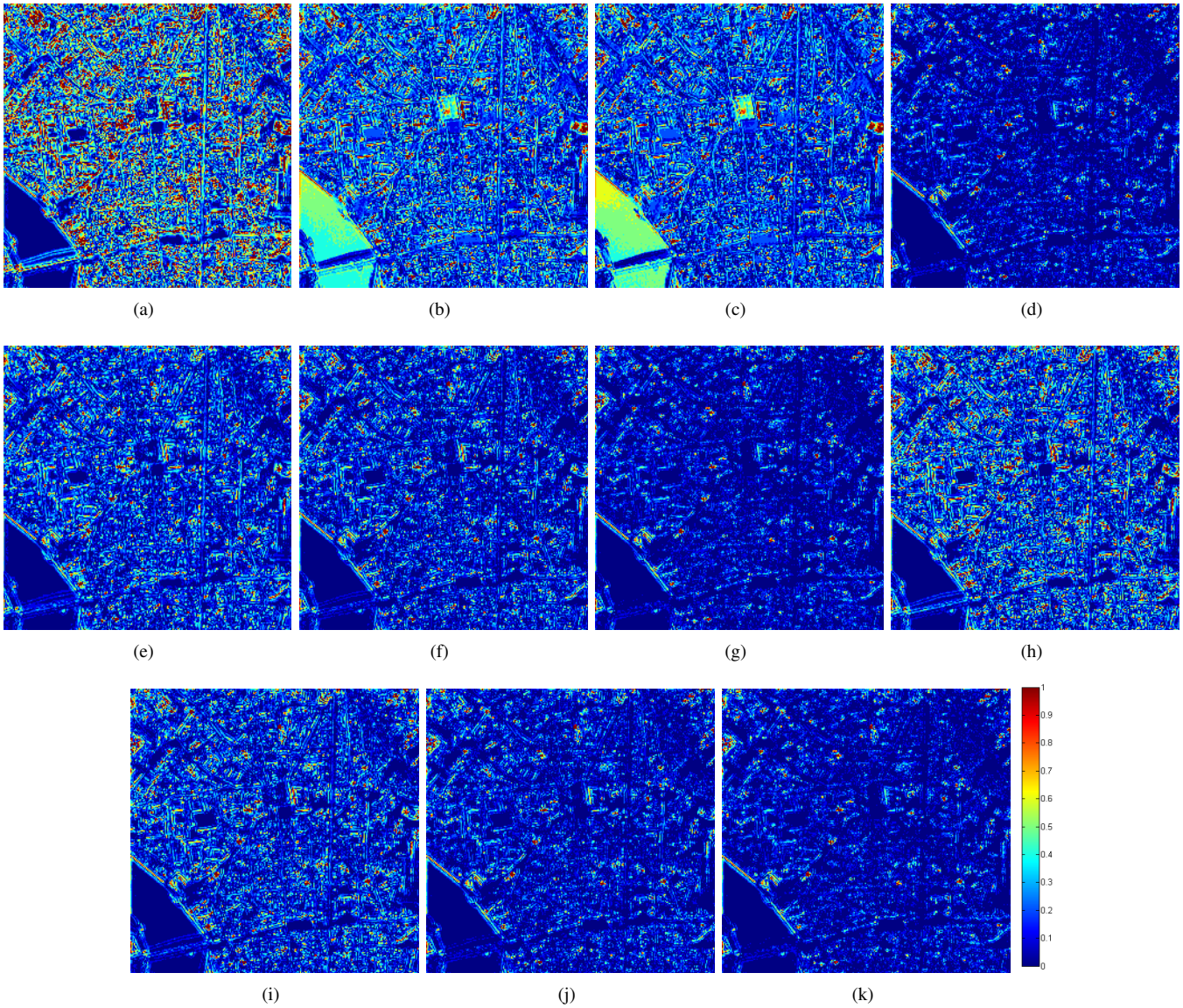

Fig. 5: Close-ups of ERGAS maps for the *Toulouse dataset* with $R = 4$: (a) EXP; (b) Brovey; (c) GS; (d) GSA; (e) SFIM; (f) GLP-HPF; (g) GLP-Reg RS; (h) GLP-Reg FS EXP; (i) GLP-Reg FS GS; (j) GLP-Reg FS GLP-HPF; k GLP-Reg FS Iterative.

i) Wald's protocol is exploited simulating products at reduced resolution with $R = 4$; ii) Full resolution assessment fusing MS and PAN at full (original) resolution. The size of the datasets in both the cases is 512×512 pixels. An overview of the used set of data is in Fig. 2.

B. Compared Algorithms

Several algorithms have been employed for comparison in this work. The MS image interpolation, using a polynomial kernel with 23 coefficients (EXP) [48], represents the baseline, since the estimation of the high resolution MS image is obtained without resorting to the companion PAN image. We selected among the CS methods some classical instances performing a global implementation of the fusion techniques, namely, the Brovey transform (Brovey) [12], the Gram-Schmidt (GS) approach [15] and the GS adaptive (GSA) technique [28], and three recently proposed approaches: the Context-adaptive Band-Dependent Spatial-Detail (C-BDSD) [47] that is based on image segmentation, the partial replacement adaptive component substitution (PRACS) [51], and the nonlinear IHS (NL-IHS) [52], which exploits an adaptive computation of the intensity image. Among the MRA algorithm we tested the smoothing filter-based intensity modulation (SFIM) approach [30], [8], the generalized Laplacian pyramid (GLP) matched with the MS sensor's modulation transfer function (MTF) with additive injection model (GLP-HPF) [48], [44], [8] and a recent implementation exploiting a nonlinear decomposition scheme using the half gradient morphological operator (MG-HF) [53]. Moreover, we included in the comparison the third generation methods implementing i) the sparse representation theory through the algorithms proposed by Zhu and Bamler (SR-

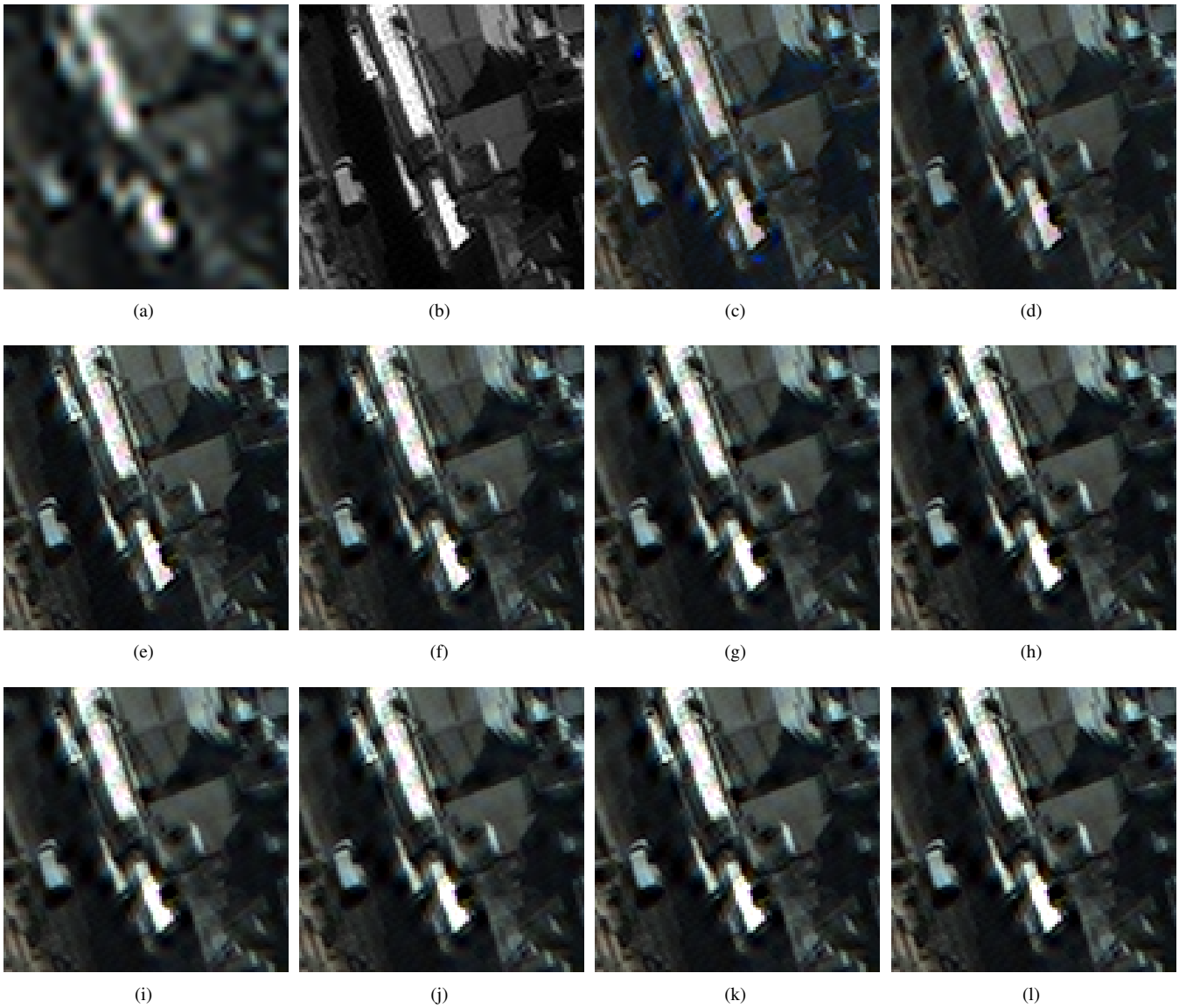

Fig. 7: Close-ups of some of the compared pansharpening approaches for the *Rio dataset* at full resolution (selected bands red, green, and blue): (a) EXP; (b) PAN; (c) Brovey; (d) GS; (e) GSA; (f) SFIM; (g) GLP-HPF; (h) GLP-Reg RS; (i) GLP-Reg FS EXP; (j) GLP-Reg FS GS; k GLP-Reg FS GLP-HPF; (l) GLP-Reg FS Iterative.

Z) in [54] and by Li, Yin and Fang (SR-L) in [21], and ii) a variational formalization for simultaneously registering and fusing the MS and the PAN images (SIRF) [55].

Finally, we assessed the proposed GLP full scale regression-based approaches with its low resolution regression-based version, the so-called GLP with context-based decision (GLP-CBD) [48], [44], [8]. From hereon, we name it *GLP-Reg RS* to point out that it is a regression-based GLP with an estimation of the injection coefficients at reduced scale (RS). The full scale regression-based GLP versions are instead called *GLP-Reg FS*, where FS stands for full scale. The two-step procedure is applied using three different guess images: i) *GLP-Reg FS EXP* uses the EXP image that represents a first, really rough, but not time-consuming, estimation of a full scale image; ii) *GLP-Reg FS GS* exploits the GS pansharpened product; whereas iii) *GLP-Reg FS GLP-HPF* is based on the GLP-HPF fusion product. Finally, the asymptotic (closed-form) expression of the proposed iterative procedure is named *GLP-Reg FS Iterative*.

C. Assessment Procedures

Quality evaluation of pansharpened image has been carried out at both reduced and full resolutions. Indeed, the reduced resolution assessment, following Wald's protocol [50], [39], [8], has as advantage the use of objective quality/distortion measurements thanks to the availability of a reference image (the original MS). The drawbacks are instead related to the implicit hypothesis of invariance among scales of the pansharpening assessment and the bias introduced by the filtering step in order to generate the reference image. These disadvantages can be overcome by exploiting a full resolution

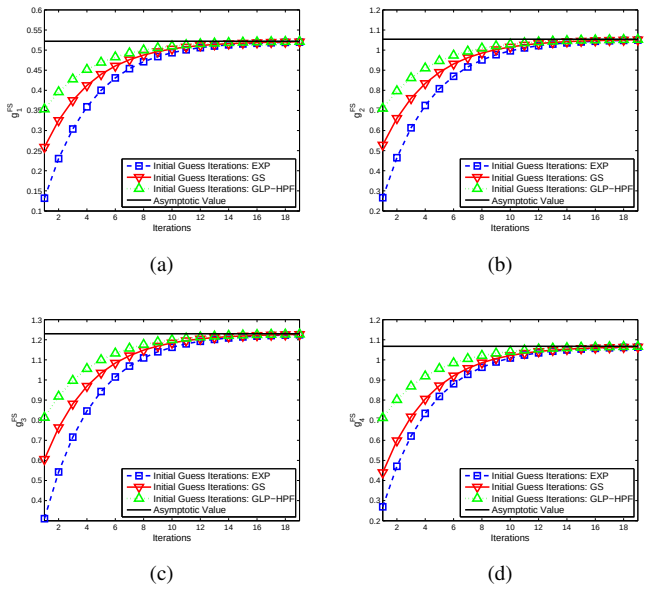

Fig. 4: Injection coefficients for the four spectral bands over iterations for the *Toulouse dataset* with $R = 8$: (a) $g_1^{FS,\cdot}$ (blue), (b) $g_2^{FS,\cdot}$ (green), (c) $g_3^{FS,\cdot}$ (red), and (d) $g_4^{FS,\cdot}$ (near-infrared).

validation, but at the price of a decrease of the overall accuracy due to the lack of a reference image.

Thus, in this section, both the validations have been exploited to properly assess the performance of the proposed approaches. Regarding the reduced resolution validation, the availability of reference originals allows for the use of widespread vectorial similarity indexes:

1) ERGAS: French acronym for Relative dimensionless global error in synthesis, ERGAS [39], [8] is a scene-global band-cumulative normalized error index based on the root mean square error of the k-th fused band to its reference. Low values of ERGAS indicate high similarity of MS data to their reference. The ideal value is zero.
2) SAM: Originally introduced for classification of hyperspectral images, the spectral angle mapper (SAM) [56], [8] denotes the absolute value of the spectral angle between two pixel vectors, usually expressed in degrees. The spatial average over the whole image is employed as a global spectral distortion and assume the ideal null value when the tested multi-component image is spectrally identical to its reference.
3) Q4/Q8: Q4 is an MS extension of the universal image quality index (UIQI), suitable for images having (up to) four bands. Q4 was introduced for quality assessment of pansharpened MS imagery [57], [8], using the representation of pixels as quaternions (four-components hyper-complex numbers). Q4 is made up of three different factors accounting for correlation, mean bias, and contrast variation of the test spectral bands with respect to their references. Since the modulus of the hyper-complex correlation coefficient measures the alignment of spectral vectors, Q4 can detect spectral distortions. Thus, both radiometric and spectral distortions can be encapsulated in a unique parameter. Values of Q4 are calculated on $N \times N$ blocks, i.e. 32×32 in this paper. Q4 is averaged over all the blocks to yield the global score index. Q4 takes values in $[0, 1]$ and is equal to 1 if and only if the test image and the reference image are identical. Q4 has been extended to images, whose number of bands is any power of two [58]; hence, the Q8 version is available for WorldView data.

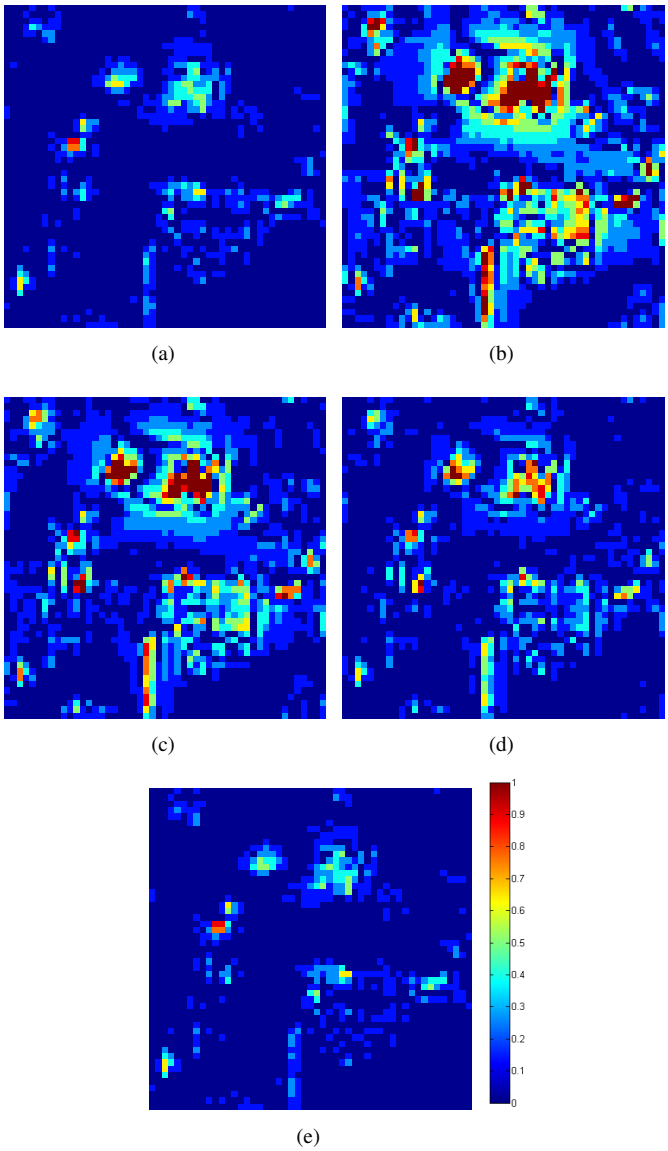

Fig. 6: Close-ups of ERGAS maps for the *Toulouse dataset* with $R = 8$: (a) GLP-Reg RS; (b) GLP-Reg FS EXP; (c) GLP-Reg FS GS; (d) GLP-Reg FS GLP-HPF; (e) GLP-Reg FS Iterative.

Regarding the full resolution validation, the *hybrid quality with no reference* (HQNR) index is exploited [59]. The HQNR index picks the best parts of two independent protocols thus being extremely accurate and reliable for translating quality trends of methods from the reduced resolution to the full

resolution. It is defined as:

$$HQNR = \left(1 - D_{\lambda}^{k}\right)^{\alpha} \left(1 - D_S\right)^{\beta}, \tag{24}$$

which is composed by the product, weighted by the coefficients α and β, of two separate values D_{λ}^{k} and D_S quantifying the spectral and the spatial distortions, respectively. The higher the HQNR index, the better the quality of the fused product. The maximum theoretical value of this index is 1 when both D_{λ}^{k} and D_S are equal to 0.

HQNR borrows the spectral distortion D_{λ}^{k} of Khan et al.'s protocol [60], which ranges in $[0, 1]$ and measures the loss of (spectral) consistency, as defined by Thomas et al.'s protocol [61]. The spatial distortion D_S is instead borrowed by the QNR index [62].

D. Results

This section is devoted to the assessment of the proposed full scale regression-based GLP approaches. The first assessment is at reduced resolution. Tabs. I and II summarize the quantitative outcomes exploiting Wald's protocol for the *Toulouse* and the *Rio* datasets.

A first remark is related to the fact that the proposed *GLP-Reg FS Iterative* gets always the best performance for all the quality indexes and datasets except in the case of the Toulouse dataset with $R = 4$ where the C-BDSD only shows slightly better performance. Furthermore, it is clear that the more the similarity between the guess image (used to estimate the injection coefficients) and the ground-truth, the better the performance obtained by the *GLP-Reg FS* approach. Indeed, we can note that for all the three test cases the ranking among the *GLP-Reg FS* methods is always the same. The worst approach is represented by the one initialized with the EXP approach (upsampled MS image). This is a time-saving approach because it does not require to fuse the MS and PAN data before applying the *GLP-Reg FS* procedure, but the outcomes produced by EXP are quite far from the ground-truth (MS image at PAN resolution). This justifies the worst performance. Higher quality products are obtained imposing the outcomes of pansharpening methods (i.e. synthetic products) as guess images. We tested two algorithms: one belonging to the CS family and one to the MRA family, i.e. GS and GLP-HPF, respectively. Better performance is remarked with respect to the initialization with EXP and the best initialization approach refers to GLP-HPF. The GS-based approach, i.e. *GLP-Reg FS GS*, is penalized by the hard spectral distortion thus getting lower performance than the *GLP-Reg FS GLP-HPF*. It is worth to be pointed out that since the guess image is used to estimate the full scale injection coefficients, the pansharpening approach used to get this synthetic data (guess image) should be designed in order to reduce the spectral distortion. Finally, we can note that the higher the quality of the guess image (measured by the overall quality index Q4/Q8), the less the gain in performance of the *GLP-Reg* procedure with respect to the starting guess. Namely, the improvement in performance that we have with the GLP-HPF is less than the one that we can get with the GS, which generally shows reduced performance.

Following this idea of having a guess image close (at least from a spectral point of view) to the ground-truth (MS image at PAN resolution) in order to estimate the injection coefficients, it is clear as the *GLP-Reg FS Iterative*, i.e. the *GLP-Reg FS* that iteratively estimates the full scale regression-based injection coefficients, obtains the best performance. Indeed, the approach gets an estimation of the injection coefficients that is better and better over the iterations, see Fig. 3, because the fused product used as guess image tends to be better and better over the iterations. In this paper, we have provided to the readers the analytic analysis of the convergence of the iterative approach (and, in particular, of its injection coefficients) for all the fusion practical cases. Furthermore, we derive the reached asymptotic values of the injection coefficients, $g_k^{FS,\infty}$ (and, thus, of the final outcome of the iterative approach), whatever the initialization of the iterative algorithm, see also the empirical validation in Fig. 4 for the *Toulouse dataset* with $R = 8$. In this section, we empirically verify it using the *Toulouse dataset* with $R = 8$, see Fig. 3. We can point out that for all the quality indexes and initializations, the iterative approach converges to the same asymptotic fused product, see (10).

The last remark about the assessment at reduced resolution is related to the comparison between the proposed full scale (*FS*) and the reduced resolution (*RS*) regression-based approaches. Tab. I summarizes the results for two ratios: $R = 4$ and $R = 8$. A greater gain in performance can be pointed out in the case of a more degraded MS image, i.e. $R = 8$ (gain of one order of magnitude assessed by the Q4s). This is justified by the considerations in the previous section. Indeed, for $R = 8$, the correlation coefficient between $\mathbf{P}_L^k$ and $\mathbf{P}^k$[3], $\rho(\mathbf{P}_L^k, \mathbf{P}^k)$, is less than the one for the case $R = 4$. We have that, for $R = 4$, $\rho(\mathbf{P}_L^k, \mathbf{P}^k) = 0.7882$, and, for $R = 8$, $\rho(\mathbf{P}_L^k, \mathbf{P}^k) = 0.6067$. This implies that more differences between the final fused products obtained by the *FS Iterative* and *RS* approaches are expected in the case $R = 8$, because $\rho(\mathbf{P}_L^k, \mathbf{P}^k)$ is farther from 1 than the case $R = 4$.

Fig. 5 shows the close-ups of the ERGAS maps for all the compared fusion products using the *Toulouse dataset* with $R = 4$. The better performance of the proposed iterative approach with respect to the state-of-the-art is clear even from a visual point of view as well as the advantages (reduction of ERGAS) with respect to the other proposed *FS* approaches that exploit a guess image to estimate the injection coefficients. Less clear is instead the visual comparison between *FS* and *RS*. Thus, the close-ups of the outcomes (ERGAS maps) for the *GLP-Reg* approaches only are depicted in Fig. 6 using the *Toulouse dataset* with $R = 8$. It can be easily seen that there is a reduction, for several pixels, of the ERGAS for *FS Iterative* (in particular compared to the one of the *RS*). In fact, it is worth to be underlined that the visual differences among these two approaches are hardly to be pointed out because they are uniformly distributed along the whole image (the unique change between the two approaches is the change in the correlation coefficient term of the injection model that influences the injection of the spatial details over the whole image).

[3]In this case, $\mathbf{P}_L^k = \mathbf{P}_L$ and $\mathbf{P}^k = \mathbf{P}$ because no preliminary equalization and no band-dependent filter are used.

			$R = 8$			$R = 4$		
	Scale	**Guess**	**SAM [°]**	**ERGAS**	**Q4**	**SAM [°]**	**ERGAS**	**Q4**
EXP			5.8078	3.4499	0.2697	4.8403	5.8793	0.5185
Brovey			5.8078	2.6727	0.7616	4.8403	4.3961	0.8152
GS			5.3546	2.5974	0.7156	4.2827	4.1701	0.8103
GSA			3.8516	1.4994	0.9104	2.9392	2.4793	0.9340
PRACS			4.7279	2.0405	0.8588	3.6299	3.3389	0.8910
C-BDSD			3.9989	1.7571	0.8878	**2.6451**	**2.3241**	**0.9366**
NLIHS			5.6456	3.1924	0.4057	4.6658	5.1663	0.6594
SFIM			4.5089	2.1412	0.7964	3.5809	3.4117	0.8742
MF-HG			3.8989	1.6913	0.8786	3.0155	2.7237	0.9200
SR-Z			4.1548	1.6589	0.8684	3.2188	2.7131	0.9183
SR-L			4.3059	2.2648	0.7303	3.3370	3.4749	0.8609
SIRF			4.7151	1.7421	0.8600	4.1479	3.4791	0.8516
GLP-HPF			4.4016	2.0476	0.8247	3.3638	3.0842	0.9052
GLP-Reg	*RS*		3.8549	1.4959	0.9109	2.9374	2.4620	0.9345
	FS	*EXP*	5.1084	2.7713	0.5845	3.8108	3.9993	0.8148
		GS	4.7708	2.2812	0.7824	3.5501	3.3947	0.8825
		GLP-HPF	4.1538	1.8204	0.8703	3.1018	2.7179	0.9245
		Iterative	**3.6509**	**1.4465**	**0.9126**	2.8451	2.4246	0.9347

TABLE I: Results for the *Toulouse dataset* for ratios R equal to 8 and 4. From the left to the right: i) pansharpening approach name; ii) scale where the injection coefficients are estimated (*RS* and *FS* stand for "reduced scale" and "full scale", respectively); iii) guess image used to estimate the coefficients at full scale; iv) performance indexes (SAM, ERGAS, and Q4). The best results are pointed out in boldface. The second best are underlined.

			Reduced Resolution Assessment			Full Resolution Assessment		
	Scale	**Guess**	**SAM [°]**	**ERGAS**	**Q8**	D_λ	D_S	**HQNR**
EXP			7.8062	10.3549	0.6808	0.0187	0.1844	0.8003
Brovey			7.8062	6.9596	0.8496	0.0536	0.0430	0.9057
GS			7.8480	6.7224	0.8650	0.0422	0.0412	0.9183
GSA			6.8267	4.9197	0.9358	0.0285	0.0171	0.9549
PRACS			7.4560	5.6822	0.9143	0.0248	0.0397	0.9364
C-BDSD			7.7527	5.6610	0.9267	0.1363	0.1644	0.7217
NLIHS			7.6020	7.4893	0.8381	0.0444	0.0555	0.9026
SFIM			6.9760	5.9083	0.9016	0.0117	0.0260	0.9626
MF-HG			6.7817	5.3383	0.9291	0.0133	0.0186	0.9684
SR-Z			8.9876	5.8989	0.9223	0.0298	0.0138	0.9568
SR-L			7.6664	6.2945	0.9082	0.0126	0.0368	0.9511
SIRF			10.2392	7.6704	0.8325	0.0159	0.0501	0.9348
GLP-HPF			6.8324	5.5495	0.9156	0.0089	0.0143	0.9769
GLP-Reg	*RS*		6.7864	4.9092	0.9357	0.0087	0.0098	0.9816
	FS	*EXP*	7.0424	6.2597	0.8919	0.0095	0.0249	0.9659
		GS	6.9416	5.7510	0.9097	0.0091	0.0182	0.9728
		GLP-HPF	6.7758	5.0667	0.9307	0.0087	0.0096	0.9818
		Iterative	**6.7685**	**4.8842**	**0.9363**	**0.0086**	**0.0090**	**0.9824**

TABLE II: Results for the *Rio dataset* (reduced and full resolution assessments). From the left to the right: i) pansharpening approach name; ii) scale where the injection coefficients are estimated (*RS* and *FS* stand for "reduced scale" and "full scale", respectively); iii) guess image used to estimate the coefficients at full scale; iv) performance indexes for reduced resolution assessment (SAM, ERGAS, and Q8); v) performance indexes for full resolution assessment (D_λ, D_S, and HQNR). The best results are pointed out in boldface. The second best are underlined.

Before ending this section, the full resolution assessment is also provided to the readers. The outcomes are summarized in Tab. II (Full Resolution Assessment) using the WorldView-3 *Rio dataset*. These results corroborate the ones obtained at reduced resolution. The HQNR indicates that the *FS Iterative* is the best approach minimizing both the spatial and spectral distortions. This approach is followed by the *FS* with GLP-HPF as guess image. A visual comparison of the fused products is also proposed and supported by the close-ups for some of the compared pansharpening approaches in Fig. 7, which confirm the outcomes obtained by the full resolution quality indexes in Tab. II (Full Resolution Assessment).

IV. Conclusions

This paper has regarded the estimation of the injection coefficients at full resolution for regression-based pansharpening approaches. For sake of brevity, we have focused attention on the powerful GLP with MTF-matched filter regression-based approach. However, all the considerations performed in this paper has been general and easily extendable to the other regression-based CS/MRA approaches. An iterative algorithm that estimates the injection coefficients at full scale has been proposed and studied. Its convergence, whatever its initialization, has been demonstrated in all the practical cases and the reached asymptotic value has been analytically

calculated. This allows us to lighten the computational burden of the approach avoiding computational demanding iterations, thus having comparable execution times with respect to the reduced scale approach.

Advantages in performance, measured at both reduced resolution (ERGAS, SAM, and Q4/Q8 indexes) and full resolution (HQNR index), with respect to the benchmark (and, in particular, to the reduced scale approach) have been shown. The good performance of the proposed approach has been shown using both four-band (IKONOS) and eight-band (WorldView-3) datasets. It is worth to be pointed out that the lower the correlation coefficient between PAN and its low resolution version (i.e. the PAN and its low resolution version strongly differ from each other), the greater the differences in performance between the estimation of the injection coefficients at reduced scale or at full scale.

APPENDIX A
RANDOM INITIALIZATION

Let us suppose that an initial guess image $\widehat{\mathbf{MS}}_k^{(0)}$ is given. Thus we can construct an improved estimate by calculating the injection coefficients as

$$g_k^{FS,0} = \frac{\operatorname{cov}(\widehat{\mathbf{MS}}_k^{(0)}, \mathbf{P}^k)}{\operatorname{var}(\mathbf{P}^k)} \tag{25}$$

and thus by defining

$$\widehat{\mathbf{MS}}_k^{(1)} = \widetilde{\mathbf{MS}}_k + g_k^{FS,0}\left(\mathbf{P}^k - \mathbf{P}_L^k\right). \tag{26}$$

The coefficient estimate can be improved by using (26), thus yielding

$$\begin{aligned} g_k^{FS,1} =& \frac{\operatorname{cov}(\widehat{\mathbf{MS}}_k^{(1)}, \mathbf{P}^k)}{\operatorname{var}(\mathbf{P}^k)} \\ =& \frac{\operatorname{cov}\left(\left[\widetilde{\mathbf{MS}}_k + g_k^{FS,0}\left(\mathbf{P}^k - \mathbf{P}_L^k\right)\right], \mathbf{P}^k\right)}{\operatorname{var}(\mathbf{P}^k)} \\ =& \frac{\operatorname{cov}\left(\widetilde{\mathbf{MS}}_k, \mathbf{P}^k\right)}{\operatorname{var}(\mathbf{P}^k)} \\ &+ \frac{\operatorname{cov}(\widehat{\mathbf{MS}}_k^{(0)}, \mathbf{P}^k)}{\operatorname{var}(\mathbf{P}^k)}\left(1 - \frac{\operatorname{cov}(\mathbf{P}_L^k, \mathbf{P}^k)}{\operatorname{var}(\mathbf{P}^k)}\right). \end{aligned} \tag{27}$$

Furthermore, the following induction step can be proved: if at iteration $n-1$ the general expression

$$\begin{aligned} g_k^{FS,n-1} =& \frac{\operatorname{cov}\left(\widetilde{\mathbf{MS}}_k, \mathbf{P}^k\right)}{\operatorname{var}(\mathbf{P}^k)} \sum_{i=0}^{n-2}\left(1 - \frac{\operatorname{cov}(\mathbf{P}_L^k, \mathbf{P}^k)}{\operatorname{var}(\mathbf{P}^k)}\right) \\ &+ \frac{\operatorname{cov}(\widehat{\mathbf{MS}}_k^{(0)}, \mathbf{P}^k)}{\operatorname{var}(\mathbf{P}^k)}\left(1 - \frac{\operatorname{cov}(\mathbf{P}_L, \mathbf{P}^k)}{\operatorname{var}(\mathbf{P}^k)}\right)^{n-1} \end{aligned} \tag{28}$$

holds, then

$$\begin{aligned} g_k^{FS,n} =& \frac{\operatorname{cov}\left(\left[\widetilde{\mathbf{MS}}_k + g_k^{FS,n-1}\left(\mathbf{P} - \mathbf{P}_L\right)\right], \mathbf{P}^k\right)}{\operatorname{var}(\mathbf{P}^k)} \\ =& \frac{\operatorname{cov}\left(\widetilde{\mathbf{MS}}_k, \mathbf{P}^k\right)}{\operatorname{var}(\mathbf{P}^k)} + \left(1 - \frac{\operatorname{cov}(\mathbf{P}_L^k, \mathbf{P}^k)}{\operatorname{var}(\mathbf{P}^k)}\right) \\ &\times \left[\frac{\operatorname{cov}\left(\widetilde{\mathbf{MS}}_k, \mathbf{P}^k\right)}{\operatorname{var}(\mathbf{P}^k)} \sum_{i=0}^{n-2}\left(1 - \frac{\operatorname{cov}(\mathbf{P}_L^k, \mathbf{P}^k)}{\operatorname{var}(\mathbf{P}^k)}\right)\right. \\ &\left. + \frac{\operatorname{cov}(\widehat{\mathbf{MS}}_k^{(0)}, \mathbf{P}^k)}{\operatorname{var}(\mathbf{P}^k)}\left(1 - \frac{\operatorname{cov}(\mathbf{P}_L, \mathbf{P}^k)}{\operatorname{var}(\mathbf{P}^k)}\right)^{n-1}\right] \\ =& \frac{\operatorname{cov}\left(\widetilde{\mathbf{MS}}_k, \mathbf{P}^k\right)}{\operatorname{var}(\mathbf{P}^k)} \sum_{i=0}^{n-1}\left(1 - \frac{\operatorname{cov}(\mathbf{P}_L^k, \mathbf{P}^k)}{\operatorname{var}(\mathbf{P}^k)}\right) \\ &+ \frac{\operatorname{cov}(\widehat{\mathbf{MS}}_k^{(0)}, \mathbf{P}^k)}{\operatorname{var}(\mathbf{P}^k)}\left(1 - \frac{\operatorname{cov}(\mathbf{P}_L^k, \mathbf{P}^k)}{\operatorname{var}(\mathbf{P}^k)}\right)^{n}. \end{aligned} \tag{29}$$

The last expression is valid for each $n \geq 1$ since (28) includes (27) for $n = 2$; thus the asymptotic value of $g_k^{FS,n}$ is given by

$$\begin{aligned} g_k^{FS,\infty} =& \lim_{n\to\infty} g_k^{FS,n} \\ =& \frac{\operatorname{cov}\left(\widetilde{\mathbf{MS}}_k, \mathbf{P}^k\right)}{\operatorname{var}(\mathbf{P}^k)} \sum_{i=1}^{\infty}\left(1 - \frac{\operatorname{cov}(\mathbf{P}_L^k, \mathbf{P}^k)}{\operatorname{var}(\mathbf{P}^k)}\right) \\ &+ \frac{\operatorname{cov}(\widehat{\mathbf{MS}}_k^{(0)}, \mathbf{P}^k)}{\operatorname{var}(\mathbf{P}^k)} \lim_{n\to\infty}\left[\left(1 - \frac{\operatorname{cov}(\mathbf{P}_L^k, \mathbf{P}^k)}{\operatorname{var}(\mathbf{P}^k)}\right)^{n}\right] \\ \overset{(a)}{=}& \frac{\operatorname{cov}(\widetilde{\mathbf{MS}}_k, \mathbf{P}^k)}{\operatorname{var}(\mathbf{P}^k)} \frac{1}{1 - \left[1 - \frac{\operatorname{cov}(\mathbf{P}_L^k, \mathbf{P}^k)}{\operatorname{var}(\mathbf{P}^k)}\right]} \\ =& \frac{\operatorname{cov}\left(\widetilde{\mathbf{MS}}_k, \mathbf{P}^k\right)}{\operatorname{cov}(\mathbf{P}_L^k, \mathbf{P}^k)}, \end{aligned} \tag{30}$$

where (a) follows if $\left|1 - \frac{\operatorname{cov}(\mathbf{P}_L^k, \mathbf{P}^k)}{\operatorname{var}(\mathbf{P}^k)}\right| < 1$, namely if (16) is valid.

REFERENCES

[1] R. A. Schowengerdt, *Remote Sensing: Models and Methods for Image Processing*, 3rd ed. Orlando, FL, USA: Elsevier, 2007.
[2] L. Alparone, B. Aiazzi, S. Baronti, and A. Garzelli, *Remote Sensing Image Fusion*. CRC Press, 2015.
[3] A. Mohammadzadeh, A. Tavakoli, and M. J. Valadan Zoej, "Road extraction based on fuzzy logic and mathematical morphology from pan-sharpened IKONOS images," *Photogramm. Rec.*, vol. 21, no. 113, pp. 44–60, Mar. 2006.
[4] I. L. Castillejo-Gonzlez, F. Lpez-Granados, A. Garca-Ferrer, J. M. Pea-Barragn, M. Jurado-Expsito, M. S. de la Orden, and M. Gonzlez-Audicana, "Object- and pixel-based analysis for mapping crops and their agro-environmental associated measures using Quickbird imagery," *Comput. Electron. Agr.*, vol. 68, no. 2, pp. 207–215, 2009.
[5] P. Sirguey, R. Mathieu, Y. Arnaud, M. M. Khan, and J. Chanussot, "Improving MODIS spatial resolution for snow mapping using wavelet fusion and ARSIS concept," *IEEE Geosci. Remote Sens. Lett.*, vol. 5, no. 1, pp. 78–82, Jan. 2008.
[6] C. Souza, Jr., L. Firestone, L. M. Silva, and D. Roberts, "Mapping forest degradation in the Eastern Amazon from SPOT 4 through spectral mixture models," *Remote Sens. Environ.*, vol. 87, no. 4, pp. 494–506, Nov. 2003.

[7] F. Bovolo, L. Bruzzone, L. Capobianco, A. Garzelli, S. Marchesi, and F. Nencini, "Analysis of the effects of pansharpening in change detection on VHR images," *IEEE Geosci. Remote Sens. Lett.*, vol. 7, no. 1, pp. 53–57, Jan. 2010.

[8] G. Vivone, L. Alparone, J. Chanussot, M. Dalla Mura, A. Garzelli, G. Licciardi, R. Restaino, and L. Wald, "A critical comparison among pansharpening algorithms," *IEEE Trans. Geosci. Remote Sens.*, vol. 53, no. 5, pp. 2565–2586, May 2015.

[9] B. Aiazzi, L. Alparone, S. Baronti, A. Garzelli, and M. Selva, "Twenty-five years of pansharpening: A critical review and new developments," in *Signal and Image Processing for Remote Sensing*, 2nd ed., C.-H. Chen, Ed. Boca Raton, FL, USA: CRC Press, 2012, pp. 533–548.

[10] H. Ghassemian, "A review of remote sensing image fusion methods," *Inform. Fusion*, vol. 32, pp. 75–89, Nov. 2016.

[11] S. Li, X. Kang, L. Fang, J. Hu, and H. Yin, "Pixel-level image fusion: A survey of the state of the art," *Inform. Fusion*, vol. 33, pp. 100–112, Jan. 2017.

[12] A. R. Gillespie, A. B. Kahle, and R. E. Walker, "Color enhancement of highly correlated images-II. Channel ratio and "Chromaticity" Transform techniques," *Remote Sens. Environ.*, vol. 22, no. 3, pp. 343–365, Aug. 1987.

[13] P. S. Chavez, Jr. and A. W. Kwarteng, "Extracting spectral contrast in Landsat Thematic Mapper image data using selective principal component analysis," *Photogramm. Eng. Remote Sens.*, vol. 55, no. 3, pp. 339–348, Mar. 1989.

[14] W. Carper, T. Lillesand, and R. Kiefer, "The use of intensity-hue-saturation transformations for merging SPOT panchromatic and multispectral image data," *Photogramm. Eng. Remote Sens.*, vol. 56, no. 4, pp. 459–467, Apr. 1990.

[15] C. A. Laben and B. V. Brower, "Process for enhancing the spatial resolution of multispectral imagery using pan-sharpening," 2000, U.S. Patent # 6,011,875.

[16] H. A. Aly and G. Sharma, "A regularized model-based optimization framework for pan-sharpening," *IEEE Trans. Image Process.*, vol. 23, no. 6, pp. 2596–2608, 2014.

[17] F. Palsson, J. R. Sveinsson, and M. O. Ulfarsson, "A new pansharpening algorithm based on total variation," *IEEE Trans. Geosci. Remote Sens.*, vol. 11, no. 1, pp. 318–322, Jan. 2014.

[18] X. He, L. Condat, J. Bioucas-Dias, J. Chanussot, and J. Xia, "A new pansharpening method based on spatial and spectral sparsity priors," *IEEE Trans. Image Process.*, vol. 23, no. 9, pp. 4160–4174, Sep. 2014.

[19] G. Vivone, M. Simões, M. Dalla Mura, R. Restaino, J. Bioucas-Dias, G. Licciardi, and J. Chanussot, "Pansharpening based on semiblind deconvolution," *IEEE Trans. Geosci. Remote Sens.*, vol. 53, no. 4, pp. 1997–2010, Apr. 2015.

[20] S. Li and B. Yang, "A new pan-sharpening method using a compressed sensing technique," *IEEE Trans. Geosci. Remote Sens.*, vol. 49, no. 2, pp. 738–746, Feb. 2011.

[21] S. Li, H. Yin, and L. Fang, "Remote sensing image fusion via sparse representations over learned dictionaries," *IEEE Trans. Geosci. Remote Sens.*, vol. 51, no. 9, pp. 4779–4789, Sep. 2013.

[22] M. R. Vicinanza, R. Restaino, G. Vivone, M. Dalla Mura, G. Licciardi, and J. Chanussot, "A pansharpening method based on the sparse representation of injected details," *IEEE Geosci. Remote Sens. Lett.*, vol. 12, no. 1, pp. 180–184, Jan. 2015.

[23] F. Fang, F. Li, C. Shen, and G. Zhang, "A variational approach for pan-sharpening," *IEEE Trans. Image Process.*, vol. 22, no. 7, pp. 2822–2834, 2013.

[24] L. V. G. Masi, D. Cozzolino and G. Scarpa, "Pansharpening by convolutional neural networks," *Remote Sens.*, vol. 8, no. 7, pp. 594–307, Jul 2016.

[25] P. S. Chavez, Jr., S. C. Sides, and J. A. Anderson, "Comparison of three different methods to merge multiresolution and multispectral data: Landsat TM and SPOT panchromatic," *Photogramm. Eng. Remote Sens.*, vol. 57, no. 3, pp. 295–303, Mar. 1991.

[26] V. K. Shettigara, "A generalized component substitution technique for spatial enhancement of multispectral images using a higher resolution data set," *Photogramm. Eng. Remote Sens.*, vol. 58, no. 5, pp. 561–567, May 1992.

[27] V. P. Shah, N. H. Younan, and R. L. King, "An efficient pan-sharpening method via a combined adaptive-PCA approach and contourlets," *IEEE Trans. Geosci. Remote Sens.*, vol. 46, no. 5, pp. 1323–1335, May 2008.

[28] B. Aiazzi, S. Baronti, and M. Selva, "Improving component substitution pansharpening through multivariate regression of MS+Pan data," *IEEE Trans. Geosci. Remote Sens.*, vol. 45, no. 10, pp. 3230–3239, Oct. 2007.

[29] A. Garzelli, F. Nencini, and L. Capobianco, "Optimal MMSE pan sharpening of very high resolution multispectral images," *IEEE Trans. Geosci. Remote Sens.*, vol. 46, no. 1, pp. 228–236, Jan. 2008.

[30] J. G. Liu, "Smoothing filter based intensity modulation: A spectral preserve image fusion technique for improving spatial details," *Int. J. Remote Sens.*, vol. 21, no. 18, pp. 3461–3472, Dec. 2000.

[31] L. Wald and T. Ranchin, "Comment: Liu 'Smoothing filter-based intensity modulation: A spectral preserve image fusion technique for improving spatial details'," *Int. J. Remote Sens.*, vol. 23, no. 3, pp. 593–597, Jan. 2002.

[32] S. Mallat, "A theory for multiresolution signal decomposition: the wavelet representation," *IEEE Trans. Pattern Anal. Mach. Intell.*, vol. 11, no. 7, pp. 674–693, Jul. 1989.

[33] G. P. Nason and B. W. Silverman, "The stationary wavelet transform and some statistical applications," in *Wavelets and Statistics*, A. Antoniadis and G. Oppenheim, Eds. New York, NY, USA: Springer-Verlag, 1995, vol. 103, pp. 281–299.

[34] M. J. Shensa, "The discrete wavelet transform: Wedding the à trous and Mallat algorithm," *IEEE Trans. Signal Process.*, vol. 40, no. 10, pp. 2464–2482, Oct. 1992.

[35] P. J. Burt and E. H. Adelson, "The Laplacian pyramid as a compact image code," *IEEE Commun. Lett.*, vol. COM–31, no. 4, pp. 532–540, Apr. 1983.

[36] M. N. Do and M. Vetterli, "The contourlet transform: An efficient directional multiresolution image representation," *IEEE Trans. Image Process.*, vol. 14, no. 12, pp. 2091–2106, Dec. 2005.

[37] J.-L. Starck, J. Fadili, and F. Murtagh, "The undecimated wavelet decomposition and its reconstruction," *IEEE Trans. Image Process.*, vol. 16, no. 2, pp. 297–309, Feb. 2007.

[38] F. Laporterie-Déjean, O. Amram, G. Flouzat, E. Pilicht, and M. Gayt, "Data fusion thanks to an improved morphological pyramid approach: comparison loop on simulated images and application to SPOT 4 data"," in *Proc. IEEE IGARSS*, 2000, pp. 2117–2119.

[39] L. Alparone, L. Wald, J. Chanussot, C. Thomas, P. Gamba, and L. M. Bruce, "Comparison of pansharpening algorithms: Outcome of the 2006 GRS-S data fusion contest," *IEEE Trans. Geosci. Remote Sens.*, vol. 45, no. 10, pp. 3012–3021, Oct. 2007.

[40] S. Baronti, B. Aiazzi, M. Selva, A. Garzelli, and L. Alparone, "A theoretical analysis of the effects of aliasing and misregistration on pansharpened imagery," *IEEE J. Sel. Topics Signal Process.*, vol. 5, no. 3, pp. 446–453, Jun. 2011.

[41] G. Vivone, R. Restaino, M. Dalla Mura, G. Licciardi, and J. Chanussot, "Contrast and error-based fusion schemes for multispectral image pansharpening," *IEEE Geosci. Remote Sens. Lett.*, vol. 11, no. 5, pp. 930–934, May 2014.

[42] B. Aiazzi, L. Alparone, S. Baronti, A. Garzelli, and M. Selva, "An MTF-based spectral distortion minimizing model for pan-sharpening of very high resolution multispectral images of urban areas," in *Proc. 2nd GRSS/ISPRS Joint Workshop Remote Sens. Data Fusion URBAN Areas*, 2003, pp. 90–94.

[43] R. Restaino, G. Vivone, M. Dalla Mura, and J. Chanussot, "Fusion of multispectral and panchromatic images based on morphological operators," *IEEE Trans. Image Process.*, vol. 25, no. 6, pp. 2882–2895, Jun. 2016.

[44] B. Aiazzi, L. Alparone, S. Baronti, A. Garzelli, and M. Selva, "MTF-tailored multiscale fusion of high-resolution MS and Pan imagery," *Photogramm. Eng. Remote Sens.*, vol. 72, no. 5, pp. 591–596, May 2006.

[45] B. Aiazzi, S. Baronti, F. Lotti, and M. Selva, "A comparison between global and context-adaptive pansharpening of multispectral images," *IEEE Trans. Geosci. Remote Sens.*, vol. 6, no. 2, pp. 302–306, Apr. 2009.

[46] R. Restaino, M. Dalla Mura, G. Vivone, and J. Chanussot, "Context-adaptive pansharpening based on image segmentation," *IEEE Trans. Geosci. Remote Sens.*, vol. 55, no. 2, pp. 753–766, Feb. 2017.

[47] A. Garzelli, "Pansharpening of multispectral images based on nonlocal parameter optimization," *IEEE Trans. Geosci. Remote Sens.*, vol. 53, no. 4, pp. 2096–2107, Apr. 2015.

[48] B. Aiazzi, L. Alparone, S. Baronti, and A. Garzelli, "Context-driven fusion of high spatial and spectral resolution images based on oversampled multiresolution analysis," *IEEE Trans. Geosci. Remote Sens.*, vol. 40, no. 10, pp. 2300–2312, Oct. 2002.

[49] L. Alparone, A. Garzelli, and G. Vivone, "Inter-sensor statistical matching for pansharpening: Theoretical issues and practical solutions," *IEEE Trans. Geosci. Remote Sens.*, vol. 55, no. 8, pp. 4682–4695, Aug. 2017.

[50] L. Wald, T. Ranchin, and M. Mangolini, "Fusion of satellite images of different spatial resolutions: Assessing the quality of resulting images," *Photogramm. Eng. Remote Sens.*, vol. 63, no. 6, pp. 691–699, Jun. 1997.
[51] J. Choi, K. Yu, and Y. Kim, "A new adaptive component-substitution-based satellite image fusion by using partial replacement," *IEEE Trans. Geosci. Remote Sens.*, vol. 49, no. 1, pp. 295–309, Jan. 2011.
[52] M. Ghahremani and H. Ghassemian, "Nonlinear IHS: A promising method for pan-sharpening," *IEEE Geosci. Remote Sens. Lett.*, vol. 13, no. 11, pp. 1606–1610, Nov. 2016.
[53] R. Restaino, G. Vivone, M. Dalla Mura, and J. Chanussot, "A pan-sharpening algorithm based on morphological filters," in *Mathematical Morphology and Its Applications to Signal and Image Processing*, J. A. Benediktsson, J. Chanussot, L. Najman, and H. Talbot, Eds. Springer, 2015, pp. 98–109.
[54] X. X. Zhu and R. Bamler, "A sparse image fusion algorithm with application to pan-sharpening," *IEEE Trans. Geosci. Remote Sens.*, vol. 51, no. 5, pp. 2827–2836, May 2013.
[55] C. Chen, Y. Li, W. Liu, and J. Huang, "SIRF: Simultaneous satellite image registration and fusion in a unified framework," *IEEE Trans. Image Process.*, vol. 24, no. 11, pp. 4213–4224, Nov. 2015.
[56] R. H. Yuhas, A. F. H. Goetz, and J. W. Boardman, "Discrimination among semi-arid landscape endmembers using the Spectral Angle Mapper (SAM) algorithm," in *Proc. Summaries 3rd Annu. JPL Airborne Geosci. Workshop*, 1992, pp. 147–149.
[57] L. Alparone, S. Baronti, A. Garzelli, and F. Nencini, "A global quality measurement of pan-sharpened multispectral imagery," *IEEE Geosci. Remote Sens. Lett.*, vol. 1, no. 4, pp. 313–317, Oct. 2004.
[58] A. Garzelli and F. Nencini, "Hypercomplex quality assessment of multi-/hyper-spectral images," *IEEE Trans. Geosci. Remote Sens.*, vol. 6, no. 4, pp. 662–665, Oct. 2009.
[59] B. Aiazzi, L. Alparone, , S. Baronti, R. Carlà, A. Garzelli, and L. Santurri, "Full scale assessment of pansharpening methods and data products," in *SPIE Remote Sensing*, 2014, pp. 924 402–924 402.
[60] M. M. Khan, L. Alparone, and J. Chanussot, "Pansharpening quality assessment using the modulation transfer functions of instruments," *IEEE Trans. Geosci. Remote Sens.*, vol. 11, no. 47, pp. 3880–3891, Nov. 2009.
[61] C. Thomas, T. Ranchin, L. Wald, and J. Chanussot, "Synthesis of multispectral images to high spatial resolution: A critical review of fusion methods based on remote sensing physics," *IEEE Trans. Geosci. Remote Sens.*, vol. 46, no. 5, pp. 1301–1312, May 2008.
[62] L. Alparone, B. Aiazzi, S. Baronti, A. Garzelli, F. Nencini, and M. Selva, "Multispectral and panchromatic data fusion assessment without reference," *Photogramm. Eng. Remote Sens.*, vol. 74, no. 2, pp. 193–200, Feb. 2008.